

1 **Complex 3D Migration and Delayed Triggering of Hydraulic Fracturing-Induced**
2 **Seismicity**

3 Dawei Gao^{1,2}, Honn Kao^{1,2*}, Bei Wang^{1,2}, Ryan Visser², Ryan Schultz³, Rebecca Harrington⁴

4
5 ¹School of Earth and Ocean Sciences, University of Victoria, Victoria, British Columbia,
6 Canada.

7 ²Pacific Geoscience Centre, Geological Survey of Canada, Sydney, British Columbia, Canada.

8 ³Department of Geophysics, Stanford University, Stanford, CA, USA.

9 ⁴Ruhr University Bochum, Institute of Geology, Mineralogy, and Geophysics, Bochum,
10 Germany.

11
12 *Corresponding author: Honn Kao (honn.kao@canada.ca)

13
14 **Key Points:**

- 15 • We document a complex 3D source migration process with delayed mainshock triggering
16 that is controlled by local hydrogeological setting.
- 17 • Poroelastic effects might contribute to induced seismicity but are insufficient to activate a
18 non-critically stressed fault of large size.
- 19 • Rapid pore-pressure build-up can be very localized and capable of producing large
20 earthquakes on non-critically stressed fault segments.

21 **Abstract**

22 Earthquakes resulting from hydraulic fracturing (HF) can have delayed triggering relative to
23 injection commencement over a varied range of time scales, with many cases exhibiting the
24 largest events near/after well completion. This poses serious challenges for risk mitigation and
25 hazard assessment. Here, we document a high-resolution, three-dimensional source migration
26 process with delayed mainshock triggering that is controlled by local hydrogeological conditions.
27 Our results reveal that poroelastic effects might contribute to induced seismicity, but are
28 insufficient to activate a non-critically stressed fault of sufficient size. The rapid pore-pressure
29 build-up from HF can be very localized and capable of producing large, felt earthquakes on non-
30 critically stressed fault segments. We interpret the delayed triggering as a manifestation of pore-
31 pressure build-up along pre-existing faults needed to facilitate seismic failure. Our findings can
32 deepen our understanding of the current stress state of crustal faults and also explain why so few
33 injection operations are seismogenic.

34

35 **Plain Language Summary**

36 Fluid injection-induced earthquakes (IIE), especially the mainshocks, are often observed to occur
37 near or after well completion. Such delayed triggering relative to injection commencement poses
38 serious challenges for both regulators and the energy industry to establish an effective mitigation
39 strategy for the potential seismic risk. In this study, we reveal a high-resolution, complex three-
40 dimensional pattern of IIE migration in Fox Creek, Alberta, Canada. The observed first-outward-
41 then-inward IIE sequence highlights the significance of hydrogeological networks in facilitating
42 fluid pressure migration and the associated seismic failure. The detailed spatiotemporal
43 distribution of IIE suggests that the effect of pore-pressure build-up from hydraulic fracturing
44 (HF) can be very localized. The delayed triggering is a combined result from the fluid pressure
45 migration and the current stress state of the hosting fault system away from the HF wells. The
46 findings from this study also provide plausible explanations on why only a very limited number
47 of fluid injections are seismogenic.

48

49

50 **1. Introduction**

51 Fluid injection-induced earthquakes (IIE), especially relatively large ones, are often observed
52 to have delayed triggering relative to injection commencement. For long-term wastewater
53 disposal (WD), the delay time can be as long as decades (*Keranen et al.*, 2013). For relatively
54 short-term hydraulic fracturing (HF) operations, the delay time varies from days to weeks. In
55 many cases, the largest events occur near or after well completion (*Schultz et al.*, 2015a, 2015b,
56 2017, 2020; *Schultz and Wang*, 2020; *Lei et al.*, 2017; *Igonin et al.*, 2020; *Wang et al.*, 2020;
57 *Peña-Castro et al.*, 2020) which severely challenges the designing of effective risk mitigation
58 strategy. Understanding the controlling factor(s) of delayed triggering of induced seismicity is of
59 paramount importance. However, the underlying physics is surprisingly far from clear due to
60 limited observations and/or incomplete injection databases.

61 The 2015 Mw 3.9 earthquake sequence near Fox Creek, Alberta, Canada is the first well-
62 known delayed HF-induced case with a ~2-week gap between the stimulation completion and the
63 mainshock. The local seismograph array data contributed by the industry enables precise
64 determination of earthquake hypocentres in comparison to other induced seismicity studies
65 which often rely on regional stations (*Bao and Eaton, 2016*). During the post-stimulation
66 process, only ~7% of the injected fluids, in contrast to a typical value of ~50% in western
67 Canada, were recovered, unambiguously indicating that a tremendous amount of fluid has leaked
68 off into nearby fault zones (*Bao and Eaton, 2016*). Given the robust earthquake locations,
69 comprehensive stimulation database, and large volume of fluid loss, the 2015 Fox Creek
70 sequence provides a unique opportunity to infer the corresponding three-dimensional (3D) fluid
71 migration process and the spatiotemporal interactions between the hosting structures and injected
72 fluid at an unprecedented resolution.

73 According to *Bao and Eaton (2016)*, the Coulomb stress change (ΔCFS) due to fracture
74 opening and pore-pressure diffusion are responsible for the earlier events that occurred during
75 the HF stimulation (referred to as the east sequence) and the delayed post-stimulation events
76 (west sequence, including the Mw 3.9 strike-slip mainshock), respectively (Figure 1a). However,
77 this model has at least two serious issues. First, it is inconsistent with the observed chronological
78 sequence of stimulation and seismicity. There are two periods of stage stimulation from north to
79 south with a ~1-week gap (Figure 1). The earliest event (i.e., the east sequence) actually occurred
80 about 2 days after the last stage of the first stimulation period (P1 in Figure 1b). This is
81 contradictory to their assumed elastic stress triggering mechanism, which should be
82 instantaneous. Instead, the 2-day delay suggests that pressure migration might have begun during
83 or shortly after P1. Moreover, the west sequence seems to initiate at greater depth relative to the
84 injection well with a clear upward trend of propagation (*Bao and Eaton, 2016*). Hence it is very
85 unlikely that the west sequence was caused by fluids from the wellbore directly above (Figure
86 1a).

87 Second, the initial model results in an overestimation of static ΔCFS in triggering the earlier
88 events (east sequence). The sudden increase of seismicity of the east sequence (including an Mw
89 3.2 earthquake) happened halfway through the second stimulation period (P2 in Figure 1b), when
90 the treatment approached the vertical fault hosting the seismicity sequence (stages 14 and 15 of
91 well 2 in Figure 1a). Thus, the actual ΔCFS in triggering these events is significantly
92 overestimated by simply summing the effects of all HF stages. Furthermore, the extremely large
93 injected volume (~50% more) and long duration (~5.75 times longer) of stage 14 compared with
94 other stages suggest the likely start time of serious fluid leakage (Figure 1b) (*Peña-Castro et al.,*
95 2020). Consequently, it is inappropriate to calculate the net ΔCFS by assuming that the total
96 fracture (opening) volume equals the total volume of injected fluid (*Bao and Eaton, 2016*).

97 Here we revisit the 2015 Fox Creek sequence with tight constraints from local geological
98 structures and injection parameters. We first employ waveform cross-correlation and hierarchical
99 clustering analysis to identify near-identical events with highly similar waveforms. The
100 distribution of these events is used to delineate the geometry of corresponding fault structures.
101 We then analyse the spatiotemporal evolution of these on-fault near-identical events. By taking
102 advantage of the complete stimulation database, we further conduct poroelastic modeling to
103 investigate the delayed triggering process. Our results reveal a high-resolution, complex 3D
104 pattern of IIE migration that is probably controlled by local fault architecture and its
105 hydrogeological properties. Finally we discuss the broad implications of this study.

106

107 **2. Methods**108 **2.1 Waveform Cross-correlation and Hierarchical Clustering Analysis**

109 Near-identical waveforms between events are commonly interpreted as indication of a similar
 110 source location and focal mechanism (*Schultz et al.*, 2014). Here we directly adopt the high
 111 accuracy earthquake catalog (69 events in total) reported in the literature (*Bao and Eaton*, 2016)
 112 and perform pair-wise waveform cross-correlation and clustering analysis (*Schultz et al.*, 2014,
 113 2015, 2017; *Hayward and Bostock*, 2017) to identify near-identical events. The cataloged events
 114 were mainly determined by local seismograph array data contributed by the industry in addition
 115 to regional seismic stations and were relocated with hypoDD (*Bao and Eaton*, 2016).

116 The waveform similarity can be quantitatively characterized by cross-correlation coefficients
 117 (CC). Since data availability of the private seismograph array used by prior work (*Bao and*
 118 *Eaton*, 2016) is restricted, we choose to calculate the CC values between event pairs with
 119 seismograms from the station BRLDA (Figure 1a) that have a generally high signal-to-noise
 120 ratio (*Schultz et al.*, 2015, 2017) and are publicly accessible from Incorporated Research
 121 Institutions for Seismology (<http://ds.iris.edu/ds/nodes/dmc/>, last accessed July 2020). The
 122 technical details of CC calculation are presented in Text S1.

123 The aforementioned pair-wise cross-correlation yields a $[69 \times 69]$ similarity matrix. We obtain
 124 the near-identical events by implementing a hierarchical clustering algorithm based on the
 125 unweighted pair-group method using the average approach (UPGMA), available as a SciPy
 126 package (*Jones et al.*, 2001, <https://docs.scipy.org>). Compared with the “chain-like” methods
 127 (e.g., *Igarashi et al.*, 2003), the UPGMA method yields more robust results in grouping
 128 earthquakes (*Hayward and Bostock*, 2017). Here we define a cluster as a group of events in
 129 which the CC of all pairs are higher than 0.75 (Figure 2a). Such a CC threshold, the same as the
 130 value used in other IIE related clustering studies (e.g., *Schultz et al.*, 2014; *Cauchie et al.*, 2020),
 131 is determined by visually inspecting the waveforms in the corresponding cluster. Eventually, we
 132 obtain 1 cluster with 20 near-identical events. The high similarity of the event waveforms,
 133 including the coda train, justifies our choice of the threshold value (Figure 2b).

134

135 **2.2 Poroelastic Modeling and ΔCFS Calculation**

136 To investigate the predominant triggering mechanism, we conduct poroelastic modeling that
 137 takes into account the interaction between pore pressure change (ΔP) and rock matrix
 138 deformation. We use the COMSOL Multiphysics® software (version 5.3a) to model the
 139 evolution of pore pressure and poroelastic stress surrounding the two HF horizontal wells.
 140 COMSOL Multiphysics® software employs the finite-element algorithm to simulate the fluid-
 141 solid coupling in a realistic scenario, thus we can estimate the pore pressure and poroelastic
 142 stress simultaneously. In this study, we apply the solid mechanism module and Darcy’s fluid
 143 flow module to simulate the coupling process. The technical details of poroelastic modeling are
 144 given in Text S2.

145 The ΔCFS has been commonly used to study the earthquake triggering process (e.g., *Stein*,
 146 1999; *Deng et al.*, 2016). After we obtain the stress tensor and pore pressure change from the
 147 COMSOL model, then we use the following equation to calculate the ΔCFS resolved on the
 148 specific fault plane (*Xu et al.*, 2010):

$$149 \quad \Delta CFS = \sin \lambda \left[\frac{-1}{2} s \dot{\phi} \sin(2\tilde{\delta}) \sigma^{11} + \frac{1}{2} \sin(2\phi) \sin(2\tilde{\delta}) \sigma^{12} + \sin \phi \cos(2\tilde{\delta}) \sigma^{13} - \frac{1}{2} \cos^2 \phi \sin(2\tilde{\delta}) \sigma^{22} - \cos \phi \sin(2\tilde{\delta}) \right]$$

150 (1)

151 where $\mu=0.6$ is the friction coefficient, ϕ , $\tilde{\delta}$, and λ are the strike, dip, and rake of the receiver
 152 fault, respectively, σ^{ij} is the stress tensor, where $i, j = 1, 2, 3$ are the 3D components in the
 153 Cartesian coordinate system, and ΔP is the pore pressure change. Based on the Coulomb failure
 154 criteria, seismic slip is promoted for a positive ΔCFS , and vice versa (King *et al.*, 1994).

155

156 3. Results

157 3.1 A High-resolution 3D Pattern of IIE Migration

158 Based on the results of waveform analysis (Section 2.1), 20 out of 69 events are found with
 159 high CC (>0.75) and near-identical waveforms, implying that they have ruptured on similar
 160 structures with similar focal mechanisms. Overall, the similarity matrix of these near-identical
 161 events shows two high CC patches (Figure 2a) – one corresponds to the earlier events in the east
 162 sequence and the other to the later events in the west sequence (Figure 3). Such a two-patch
 163 pattern is consistent with the two main near-vertical fault structures (Figure 3) inferred from
 164 earthquake focal mechanisms (Schultz *et al.*, 2017). According to the “flower structure” model,
 165 these two near-vertical faults may merge together in the basement (Wang *et al.*, 2017). The
 166 remaining 49 poorly correlated events are generally small (overall $M_w \leq 1$, Figure S1) and likely
 167 to have occurred on the nearby tiny fractures with possibly different orientations and/or focal
 168 mechanisms.

169 It is worth noting that the event magnitudes increase with focal depth for both the east and
 170 west sequences (Figure 3). The overall pattern of relative location among hypocenters should be
 171 very robust as they are determined by the high-resolution double-difference method (Waldhauser
 172 and Ellsworth, 2000) with data from a local seismic array established by the private industry
 173 (Bao and Eaton, 2016). Most of the largest events appear to have occurred near/in the crystalline
 174 basement, possibly due to the varied degrees of fault maturity at different depths (Kozłowska *et al.*
 175 *et al.*, 2018). In comparison, there is no significant event immediately above or below the HF-
 176 targeted Duvernay shale formation (Figure 3). It appears that the aseismic region can extend up
 177 to 200 m surrounding the horizontal wells (Guglielmi *et al.*, 2015; Eyre *et al.*, 2019a).

178 The spatiotemporal evolution of the near-identical on-fault events (colored circles in Figure 3)
 179 clearly shows how the seismicity migrates in a 3D way: first in the east from shallow to deep,
 180 then shifting to the west, finally from deep to shallow. The seismicity migration, along with the
 181 huge fluid loss (Bao and Eaton, 2016), inherently implies the migration of the leaked fluid along
 182 pre-existing geological faults. Although the east sequence falls out of the target fracturing region
 183 (which is usually within a few hundred meters of the well), it is highly likely that a direct fluid
 184 connection exists between the injection well and triggered seismicity through permeable
 185 pathways. Such an inference is supported by many other cases documented in the literature (e.g.,
 186 Wolhart *et al.*, 2005; Davies *et al.*, 2013; Galloway *et al.*, 2018; Igonin *et al.*, 2020) where the
 187 maximum fluid communication distance can be as far as ~ 1 km (Wilson *et al.*, 2018; Igonin *et al.*
 188 *et al.*, 2020; Fu and Dehghanpour, 2020). The uppermost part of the east sequence fault seems to
 189 be aseismic, possibly due to the close proximity to the injection area (Guglielmi *et al.*, 2015; De
 190 Barros *et al.*, 2016) and/or high clay and organic content in the shale formation that favors stable
 191 sliding (Kohli and Zoback, 2013; Eyre *et al.*, 2019a). Upon fluid injection, the fault permeability
 192 in the vicinity of fluid channel may increase dramatically during the aseismic period (Guglielmi
 193 *et al.*, 2015) which, in turn, facilitates rapid downward fluid pressure migration, eventually
 194 leading to seismic failures towards the basement. The fluid then migrates from east to west

195 through faults in the basement as evident from the timing and location of the induced seismicity.
 196 Finally the fluid pressure may migrate vertically (*Birdsell et al.*, 2015) along the west sequence
 197 fault hinted by the seismicity pattern (*Haagenson and Rajaram*, 2020). A lack of typical Omori-
 198 type aftershock sequences after the Mw 3.9 event on the west sequence fault (*Bao and Eaton*,
 199 2016) provides another piece of evidence of the involvement of an external force (fluid pressure)
 200 (*Lei et al.*, 2017; 2019) and thus explains the fluid's origin (from the east) and upward
 201 earthquake migration on the west.

202 In summary, in contrast to the conventional wisdom that the geomechanical effects due to
 203 fluid injection migrate outward from the injection site, our results reveal a high-resolution,
 204 complex 3D pattern of IIE migration that can go both outward and inward as controlled by local
 205 fault architecture and its hydrogeological properties. The pore pressure build-up due to rapid
 206 fluid pressure migration has caused the Mw 3.2 earthquake on the east sequence fault and Mw
 207 3.9 event on the west (Figure 3). This first-outward-then-inward sequence highlights the
 208 significance of hydrologic networks in facilitating fluid pressure migration and the associated
 209 seismic failure. However, event No. 1 (Mw 1.98) appears to be an exception. It occurred very
 210 early (soon after the start of stage 17 of well 2 in P2, Figure 1b), not on the east sequence fault
 211 but on the west. The hypocenter is close to event No. 11 as evident by both high CC values
 212 (Figure 2a) and precise hypocentre locations (Figure 3). Given the timing and location, event No.
 213 1 may have been caused by poroelastic effects rather than a pore pressure perturbation.

214

215 **3.2 Delayed Triggering Due to Pore Pressure Build-up**

216 We verify the hypothesis of the pore pressure build-up being the predominant triggering
 217 mechanism through poroelastic modeling (Section 2.2). In the model, we consider two scenarios
 218 for the east sequence fault: one where the near-vertical east sequence fault intersects the inferred
 219 horizontal fluid channel, and the other where it does not (Figure 3). Our model results indicate
 220 that the ΔCFS due to poroelastic effects alone (i.e., without hydrologic communication) is only
 221 ~ 0.06 bar (Figure 4a). Such a small change is likely insufficient to trigger the Mw 3.2 event on
 222 the east sequence fault as it is significantly below the triggering threshold (0.2 bar) adopted by
 223 previous studies (e.g., *Fischer et al.*, 2008; *Wang et al.*, 2021). Instead, allowing fluid pressure
 224 migration to the seismogenic east sequence fault can explain the observations very well. Figure
 225 4a clearly shows that the ΔP dominates the ΔCFS in elevating stress to sufficient levels to cause
 226 the Mw 3.2 event. We also tested a range of physically reasonable permeability values (*Cappa*,
 227 2009; *Farrel and Taylor*, 2014) for the inferred near-horizontal basement fault that facilitates
 228 rapid fluid pressure migration from the east sequence fault towards the west. A minimum
 229 permeability of 4×10^{-14} m², about 4 orders higher than that of the low-permeability country rock
 230 (10^{-18} m², Table S1), is found to be required to cause seismic failures on the west sequence fault
 231 for the observed time scale (Figure 4b). Such a high permeability value is consistent with the
 232 laboratory results of well-developed fault damage zones ($10^{-16} - 10^{-14}$ m²) that lead to rapid fluid
 233 flow (*Evans et al.*, 1997). Thus, we conclude that the pore pressure build-up associated with fluid
 234 pressure migration is the key mechanism that triggered the 2015 Fox Creek earthquake sequence,
 235 and that the complex 3D spatiotemporal pattern of hypocenters is dictated by the local
 236 hydrogeological setting. Our results also demonstrate that local hydrological pathways, fault
 237 structures, and a complete stimulation database (e.g., accurate stage timing and volume) must all
 238 be properly incorporated in the modeling to avoid incorrect outcomes and misinterpretation (*Bao*
 239 *and Eaton*, 2016).

240

241 **4. Interpretation and Implications**

242 **4.1 Reactivation of A Non-critically Stressed Fault Segment**

243 Previous studies have suggested that the hosting fault must be critically stressed for relatively
 244 large ($M > 2$) IIE to occur (*Atkinson et al.*, 2020). However, our observations suggest that the east
 245 sequence fault was not critically stressed before stimulation, as no event was triggered by
 246 poroelastic effects when the stage stimulation started. Instead, the largest event in the east
 247 sequence (event No. 7) occurred ~ 3 days after event No. 0 (Figure 1b). The ~ 3 -day delay time
 248 suggests that stage stimulation can dramatically alter the stress state from non-critical to critical
 249 over an extremely short period (on the order of days), in contrast to the tectonic loading cycle (on
 250 the order of tens/hundreds of years).

251 Another hint of reactivating a non-critically stressed fault by HF comes from the west
 252 sequence fault that hosts the 2015 Mw 3.9 event. About one year later, another comparable-sized
 253 event (Mw 4.1) was also induced by HF slightly to the south (Figure 1a; *Wang et al.*, 2017; *Eyre*
 254 *et al.*, 2019a, b). These two events share near-identical focal mechanisms (Figure 1a) and
 255 waveforms (Figure 2b), have adjacent locations (epicenters less than 1.5 km apart, and similar
 256 depths within ~ 1 km; *Schultz et al.*, 2017, *Eyre et al.*, 2019b), and both occurred after the
 257 completion of HF operations with potentially significant fluid leakage (*Bao and Eaton*, 2016;
 258 *Eyre et al.*, 2019b). Thus, the two large events are most likely to have occurred on two adjacent
 259 segments of the same N-S striking fault. Having two nearby ruptures of limited size instead of
 260 rupturing the whole west sequence fault at once suggests that the hosting fault is well below the
 261 critical state. This inference is also supported by a recent slip tendency analysis (*Shen et al.*,
 262 2019). Our observations indicate that the effect of HF stimulation can be very localized for a
 263 non-critically stressed fault given the relatively small injected volume. Therefore, it can only
 264 elevate the stress state of a limited segment of the hosting fault to facilitate seismic failure.

265

266 **4.2 Current Stress State of Crustal Faults**

267 Our observations clearly show that both the east and west sequence faults were not critically
 268 stressed before stimulation, as no large earthquakes occurred at the very beginning of stimulation
 269 and/or were caused by poroelastic effects. Furthermore, the west sequence fault hosted two large
 270 earthquakes of comparable size on neighbouring segments instead of rupturing the whole fault at
 271 once. Considering the facts that (i) most injection operations are not seismogenic (*Atkinson et al.*,
 272 2016; *Schultz et al.*, 2017, 2020; *Rubinstein and Mahani*, 2015; *Weingarten et al.*, 2015), (ii)
 273 events triggered by poroelastic effects are usually of small magnitudes (*Deng et al.*, 2016;
 274 *Kozłowska et al.*, 2018; *Yu et al.*, 2019), (iii) the elevation of pore pressure is widely considered
 275 to be the primary cause of relatively large IIE (*Lei et al.*, 2019; *Peña-Castro et al.*, 2020; *Wang*
 276 *et al.*, 2021; *Schultz and Wang*, 2020), and (iv) for the majority of HF-induced IIE cases, the
 277 largest events often occur near or after well completion (*Schultz et al.*, 2015a, 2015b, 2017;
 278 *Schultz and Wang*, 2020; *Lei et al.*, 2017; *Igonin et al.*, 2020; *Wang et al.*, 2020; *Peña-Castro et*
 279 *al.*, 2020), we infer that the number of critically stressed, large intraplate faults should be very
 280 limited, and that reactivation of such faults requires sufficient pore-pressure accumulation.

281

282 **4.3 Delayed Triggering of IIE**

283 Taking advantage of the high-resolution distribution of hypocentres and complete HF
 284 stimulation database, our study reveals that a complex 3D source migration process with the
 285 delay of large earthquakes is controlled by the local hydrogeological setting. Numerical
 286 modeling demonstrates that poroelastic effects alone (i.e., without direct hydrological
 287 connection) are insufficient to activate the east sequence fault. Instead, the delayed occurrence of
 288 two relatively large events (i.e., Mw 3.2 and Mw 3.9) on the time scale of days to weeks can be
 289 well-explained by the pore-pressure build-up along the complex local fault system involving an
 290 initially outward path at the shallow depth and a later inward one at a greater depth. Although the
 291 actual fluid channel and fault architecture could be even more complicated than what we have
 292 assumed (Figure 3), our model succeeds in explaining the IIE migration process to the first order.

293 Therefore, the complexity of the hydrologic network determines whether and how fast the
 294 fluid can reach the fault; and the current stress state of the hosting fault determines how long it
 295 takes for pore-pressure build-up to facilitate seismic failure. This might explain why no large IIE
 296 thus far occur at the onset of HF stimulation. Instead, they tend to occur near the end of, or even
 297 after the stage stimulation with a wide range of time delays (*Schultz et al.*, 2015a, 2015b, 2017;
 298 *Schultz and Wang*, 2020; *Lei et al.*, 2017; *Igonin et al.*, 2020; *Wang et al.*, 2020; *Peña-Castro et*
 299 *al.*, 2020).

300

301 **4.4 Seismogenic vs. Aseismogenic Injection Operations**

302 Direct fluid communication should be geologically rare (*Galloway et al.*, 2018). Whether
 303 earthquakes can be triggered by an injection operation depends on: (i) the probability of
 304 connecting the injection to a pre-existing seismogenic fault, and (ii) whether the amount of
 305 injected fluid is sufficient to bring the fault to critical state. Even if direct fluid communication
 306 exists, the largest magnitude of triggered events will depend on both the dimension of the pre-
 307 existing fault and the cumulative volume of injected fluid (*Schultz et al.*, 2018). Meeting all these
 308 conditions may be statistically demanding, and thus can explain why the majority of seismogenic
 309 wells do not produce large felt IIE. This essentially agrees with the Gutenberg-Richter law that
 310 smaller earthquakes occur much more frequently than the larger ones.

311

312 **5. Discussion and Conclusions**

313 Waveform similarity has been a powerful seismological tool recently to study earthquake
 314 source characteristics (*Schultz et al.*, 2014, 2020). While there are increasing evidences that
 315 waveform CC alone cannot reliably distinguish repeating earthquakes from neighboring events
 316 (e.g., *Ellsworth and Bulut*, 2018), nearly identical waveforms are useful in identifying nearby
 317 earthquakes with similar focal mechanisms. In fact, using single-station CC values to identify
 318 earthquakes with similar origins has been a common practice in previous studies, especially for
 319 areas with limited station availability (e.g., *Li and Richards*, 2003; *Schaff and Richards*, 2004; *Li*
 320 *et al.*, 2011; *Buurman et al.*, 2013; *Schultz et al.*, 2014, 2015, 2017; *Yamada et al.*, 2016;
 321 *Hayward and Bostock*, 2017; *Cauchie et al.*, 2020; *Gao and Kao*, 2020). We have tried different
 322 CC threshold values in our hierarchical clustering analysis, and the results are all similar.
 323 Although our cross-correlation and clustering analysis are based on single-station data, the
 324 overall match of the similarity matrix of the near-identical events (Figure 2a) and their
 325 hypocenter locations (Figure 3) demonstrate the effectiveness of our approach.

326 We take a more conservative approach in the investigation of the predominant triggering
 327 mechanism of IIE by assuming a triggering threshold of $\Delta CFS = 0.2$ bar (e.g., *Fischer et al.*,

2008; Wang *et al.*, 2021). Some studies have considered a lower value of 0.1 bar to define the triggering threshold (e.g., Stein, 1999; King *et al.*, 1994). Regardless which triggering threshold (0.1 or 0.2 bar) is used, the ΔCFS due to poroelastic effects alone is much smaller (0.06 bar, Figure 4a) and hence is insufficient to trigger the Mw 3.2 event on the east sequence fault. We conclude that the poroelastic effects are at most a contributor in triggering the Mw 3.2 mainshock, whereas rapid pore-pressure build-up through permeable pathways may play a more important role.

To summarize, our study reveals that (i) poroelastic effects of HF stimulation might contribute to the occurrence of IIE, but are insufficient to activate a non-critically stressed fault segment of sufficient size, (ii) the effect of HF can be very localized and non-critically stressed fault segments can produce large felt IIE with rapid pore-pressure build-up, and (iii) the spatiotemporal distribution of IIE can exhibit a very complicated 3D pattern depending on the specific local hydrogeological setting. Therefore, mapping pre-existing geological faults and avoiding direct hydrologic connection to them may be of paramount importance in mitigating short-term seismic hazard from IIE. Precise and accurate assessment of the state of stress of local fault systems is probably the key step in the strategy of maximizing the economic benefit of HF operations and minimizing the potential impact to the safety of local communities and infrastructure.

Acknowledgements

Insightful discussions with Fengzhou Tan, Ramin Mohammad Hosseini Dokht, Yajing Liu, and Stan Dosso are much appreciated. Waveform data used in this study were downloaded from the Incorporated Research Institutions for Seismology (<http://ds.iris.edu/ds/nodes/dmc/>, last accessed July 2020). Seismic data are processed with Obspy (Beyreuther *et al.*, 2010). Figures are made with Matplotlib (Hunter, 2007) and Inkscape (<https://inkscape.org>). This study is partially supported by a University of Victoria Fellowship (DG), the Induced Seismicity Research Project of NRCan (HK), Geoscience BC (HK), and a NSERC Discovery Grant (HK). This paper is NRCan contribution 2021xxxx.

References

- Atkinson, G. M., Eaton, D. W., & Igonin, N. (2020). Developments in understanding seismicity triggered by hydraulic fracturing. *Nature Reviews Earth & Environment*, 1-14.
- Atkinson, G. M., Eaton, D. W., Ghofrani, H., Walker, D., Cheadle, B., Schultz, R., ... & Kao, H. (2016). Hydraulic fracturing and seismicity in the Western Canada Sedimentary Basin. *Seismological research letters*, 87(3), 631-647.
- Bao, X., & Eaton, D. W. (2016). Fault activation by hydraulic fracturing in western Canada. *Science*, 354(6318), 1406-1409.
- Beyreuther, M., Barsch, R., Krischer, L., Megies, T., Behr, Y., & Wassermann, J. (2010). ObsPy: A Python toolbox for seismology. *Seismological Research Letters*, 81(3), 530-533.
- Birdsell, D. T., Rajaram, H., Dempsey, D., & Viswanathan, H. S. (2015). Hydraulic fracturing fluid migration in the subsurface: A review and expanded modeling results. *Water Resources Research*, 51(9), 7159-7188.

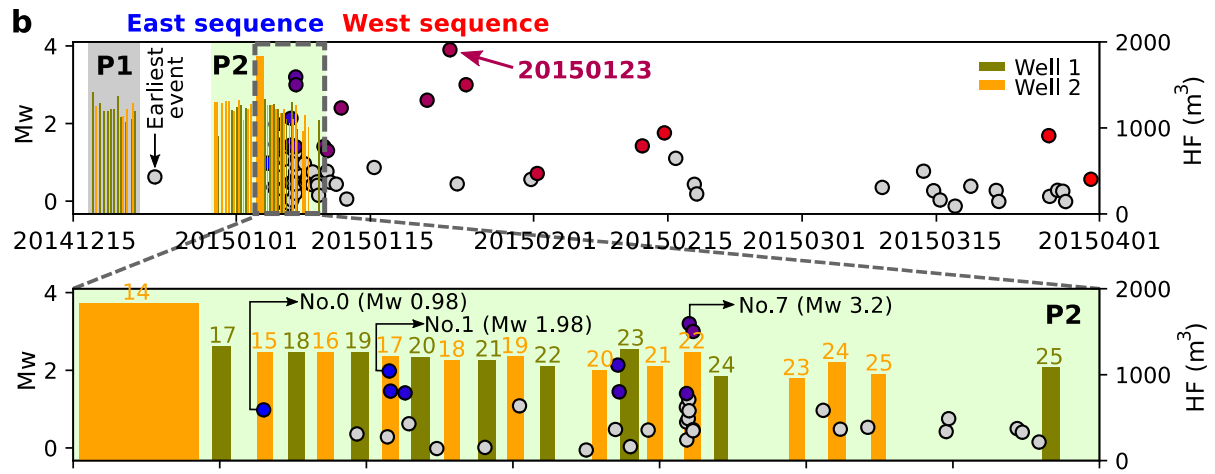
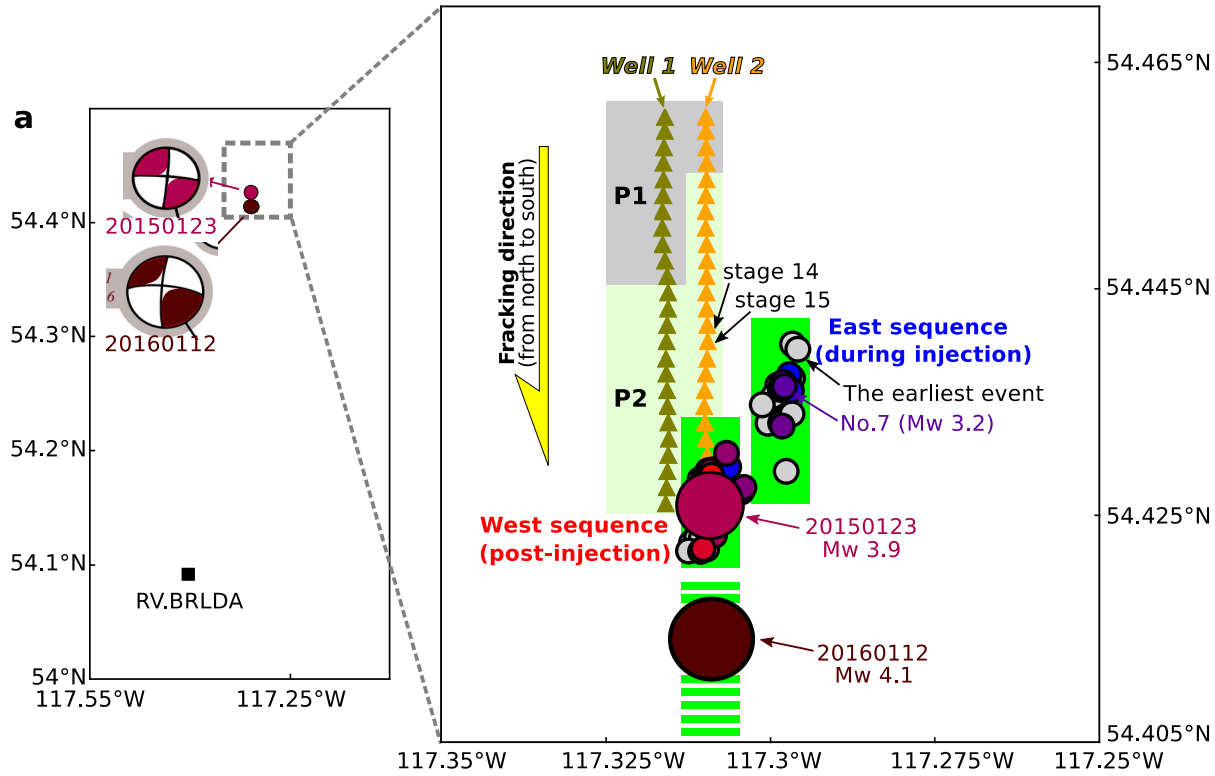
- 370 Buurman, H., West, M. E., & Thompson, G. (2013). The seismicity of the 2009 Redoubt
 371 eruption. *Journal of Volcanology and Geothermal Research*, 259, 16-30.
- 372 Cappa, F. (2009). Modelling fluid transfer and slip in a fault zone when integrating
 373 heterogeneous hydromechanical characteristics in its internal structure. *Geophysical Journal*
 374 *International*, 178(3), 1357-1362.
- 375 Cauchie, L., Lengliné, O., & Schmittbuhl, J. (2020). Seismic asperity size evolution during fluid
 376 injection: case study of the 1993 Soultz-sous-Forêts injection. *Geophysical Journal*
 377 *International*, 221(2), 968-980.
- 378 Davies, R., Foulger, G., Bindley, A., & Styles, P. (2013). Induced seismicity and hydraulic
 379 fracturing for the recovery of hydrocarbons. *Marine and petroleum geology*, 45, 171-185.
- 380 De Barros, L., Daniel, G., Guglielmi, Y., Rivet, D., Caron, H., Payre, X., ... & Gourlay, M.
 381 (2016). Fault structure, stress, or pressure control of the seismicity in shale? Insights from a
 382 controlled experiment of fluid-induced fault reactivation. *Journal of Geophysical Research:*
 383 *Solid Earth*, 121(6), 4506-4522.
- 384 Deng, K., Liu, Y., & Harrington, R. M. (2016). Poroelastic stress triggering of the December
 385 2013 Crooked Lake, Alberta, induced seismicity sequence. *Geophysical Research*
 386 *Letters*, 43(16), 8482-8491.
- 387 Ellsworth, W. L., & Bulut, F. (2018). Nucleation of the 1999 Izmit earthquake by a triggered
 388 cascade of foreshocks. *Nature Geoscience*, 11(7), 531-535.
- 389 Evans, J. P., Forster, C. B., & Goddard, J. V. (1997). Permeability of fault-related rocks, and
 390 implications for hydraulic structure of fault zones. *Journal of structural Geology*, 19(11),
 391 1393-1404.
- 392 Eyre, T. S., Eaton, D. W., Garagash, D. I., Zecevic, M., Venieri, M., Weir, R., & Lawton, D. C.
 393 (2019a). The role of aseismic slip in hydraulic fracturing-induced seismicity. *Science*
 394 *advances*, 5(8), eaav7172.
- 395 Eyre, T. S., Eaton, D. W., Zecevic, M., D'Amico, D., & Kolos, D. (2019b). Microseismicity
 396 reveals fault activation before M w 4.1 hydraulic-fracturing induced earthquake. *Geophysical*
 397 *Journal International*, 218(1), 534-546.
- 398 Farrell, N. J. C., Healy, D., & Taylor, C. W. (2014). Anisotropy of permeability in faulted porous
 399 sandstones. *Journal of Structural Geology*, 63, 50-67.
- 400 Fischer, A. D., Peng, Z., & Sammis, C. G. (2008). Dynamic triggering of high-frequency bursts
 401 by strong motions during the 2004 Parkfield earthquake sequence. *Geophysical Research*
 402 *Letters*, 35(12).
- 403 Fu, Y., & Dehghanpour, H. (2020). How far can hydraulic fractures go? A comparative analysis
 404 of water flowback, tracer, and microseismic data from the Horn River Basin. *Marine and*
 405 *Petroleum Geology*, 115, 104259.
- 406 Galloway, E., Hauck, T., Corlett, H., Pană, D., & Schultz, R. (2018). Faults and associated karst
 407 collapse suggest conduits for fluid flow that influence hydraulic fracturing-induced
 408 seismicity. *Proceedings of the National Academy of Sciences*, 115(43), E10003-E10012.

- 409 Gao, D., & Kao, H. (2020). Optimization of the Match–Filtering Method for Robust Repeating
 410 Earthquake Detection: The Multisegment Cross–Correlation Approach. *Journal of*
 411 *Geophysical Research: Solid Earth*, 125(7), e2020JB019714.
- 412 Guglielmi, Y., Cappa, F., Avouac, J. P., Henry, P., & Elsworth, D. (2015). Seismicity triggered
 413 by fluid injection–induced aseismic slip. *Science*, 348(6240), 1224-1226.
- 414 Haagensohn, R., & Rajaram, H. (2020). Seismic diffusivity: The influence of fracture networks on
 415 the patterns of induced seismicity. In *EGU General Assembly Conference Abstracts* (p.
 416 20308).
- 417 Hayward, T. W., & Bostock, M. G. (2017). Slip behavior of the queen Charlotte plate boundary
 418 before and after the 2012, MW 7.8 Haida Gwaii earthquake: evidence from repeating
 419 earthquakes. *Journal of Geophysical Research: Solid Earth*, 122(11), 8990-9011.
- 420 Hunter, J. D. (2007). Matplotlib: A 2D graphics environment. *Computing in science &*
 421 *engineering*, 9(3), 90-95.
- 422 Igarashi, T., Matsuzawa, T., & Hasegawa, A. (2003). Repeating earthquakes and interplate
 423 aseismic slip in the northeastern Japan subduction zone. *Journal of Geophysical Research:*
 424 *Solid Earth*, 108(B5).
- 425 Igonin, N., Verdon, J. P., Kendall, J. M., & Eaton, D. W. (2020). Large–scale fracture systems
 426 are permeable pathways for fault activation during hydraulic fracturing. *Journal of*
 427 *Geophysical Research: Solid Earth*, e2020JB020311.
- 428 Jones, E., Oliphant, T., & Peterson, P. (2001). SciPy: Open source scientific tools for Python.
- 429 Kennett, B. L., Engdahl, E. R., & Buland, R. (1995). Constraints on seismic velocities in the
 430 Earth from traveltimes. *Geophysical Journal International*, 122(1), 108-124.
- 431 Keranen, K. M., Savage, H. M., Abers, G. A., & Cochran, E. S. (2013). Potentially induced
 432 earthquakes in Oklahoma, USA: Links between wastewater injection and the 2011 Mw 5.7
 433 earthquake sequence. *Geology*, 41(6), 699-702.
- 434 King, G. C., Stein, R. S., & Lin, J. (1994). Static stress changes and the triggering of
 435 earthquakes. *Bulletin of the Seismological Society of America*, 84(3), 935-953.
- 436 Kohli, A. H., & Zoback, M. D. (2013). Frictional properties of shale reservoir rocks. *Journal of*
 437 *geophysical research: solid earth*, 118(9), 5109-5125.
- 438 Kozłowska, M., Brudzinski, M. R., Friberg, P., Skoumal, R. J., Baxter, N. D., & Currie, B. S.
 439 (2018). Maturity of nearby faults influences seismic hazard from hydraulic
 440 fracturing. *Proceedings of the National Academy of Sciences*, 115(8), E1720-E1729.
- 441 Lei, X., Huang, D., Su, J., Jiang, G., Wang, X., Wang, H., ... & Fu, H. (2017). Fault reactivation
 442 and earthquakes with magnitudes of up to Mw4. 7 induced by shale-gas hydraulic fracturing
 443 in Sichuan Basin, China. *Scientific reports*, 7(1), 1-12.
- 444 Lei, X., Wang, Z., & Su, J. (2019). The December 2018 ML 5.7 and January 2019 ML 5.3
 445 earthquakes in South Sichuan basin induced by shale gas hydraulic fracturing. *Seismological*
 446 *Research Letters*, 90(3), 1099-1110.
- 447 Li, A., & Richards, P. G. (2003). Using earthquake doublets to study inner core rotation and
 448 seismicity catalog precision. *Geochemistry, Geophysics, Geosystems*, 4(9).

- 449 Li, L., Chen, Q. F., Niu, F., & Su, J. (2011). Deep slip rates along the Longmen Shan fault zone
 450 estimated from repeating microearthquakes. *Journal of Geophysical Research: Solid*
 451 *Earth*, 116(B9).
- 452 Lockner, D. A., & Beeler, N. M. (1999). Premonitory slip and tidal triggering of
 453 earthquakes. *Journal of Geophysical Research: Solid Earth*, 104(B9), 20133-20151.
- 454 Peña Castro, A. F., Roth, M. P., Verdecchia, A., Onwuemeka, J., Liu, Y., Harrington, R. M., ...
 455 & Kao, H. (2020). Stress Chatter via Fluid Flow and Fault Slip in a Hydraulic Fracturing-
 456 Induced Earthquake Sequence in the Montney Formation, British Columbia. *Geophysical*
 457 *Research Letters*, 47(14), e2020GL087254.
- 458 Rubinstein, J. L., & Mahani, A. B. (2015). Myths and facts on wastewater injection, hydraulic
 459 fracturing, enhanced oil recovery, and induced seismicity. *Seismological Research*
 460 *Letters*, 86(4), 1060-1067.
- 461 Schaff, D. P., & Richards, P. G. (2004). Repeating seismic events in China. *Science*, 303(5661),
 462 1176-1178.
- 463 Schmittbuhl, J., Karabulut, H., Lengliné, O., & Bouchon, M. (2016). Long-lasting seismic
 464 repeaters in the Central basin of the Main Marmara fault. *Geophysical Research*
 465 *Letters*, 43(18), 9527-9534.
- 466 Schultz, R., & Wang, R. (2020). Newly emerging cases of hydraulic fracturing induced
 467 seismicity in the Duvernay East Shale Basin. *Tectonophysics*, 228393.
- 468 Schultz, R., Atkinson, G., Eaton, D. W., Gu, Y. J., & Kao, H. (2018). Hydraulic fracturing
 469 volume is associated with induced earthquake productivity in the Duvernay
 470 play. *Science*, 359(6373), 304-308.
- 471 Schultz, R., Stern, V., Novakovic, M., Atkinson, G., & Gu, Y. J. (2015a). Hydraulic fracturing
 472 and the Crooked Lake sequences: Insights gleaned from regional seismic
 473 networks. *Geophysical Research Letters*, 42(8), 2750-2758.
- 474 Schultz, R., Mei, S., Paná, D., Stern, V., Gu, Y. J., Kim, A., & Eaton, D. (2015b). The Cardston
 475 earthquake swarm and hydraulic fracturing of the Exshaw Formation (Alberta Bakken
 476 play). *Bulletin of the Seismological Society of America*, 105(6), 2871-2884.
- 477 Schultz, R., Skoumal, R. J., Brudzinski, M. R., Eaton, D., Baptie, B., & Ellsworth, W. (2020).
 478 Hydraulic fracturing-induced seismicity. *Reviews of Geophysics*, 58(3), e2019RG000695.
- 479 Schultz, R., Stern, V., & Gu, Y. J. (2014). An investigation of seismicity clustered near the
 480 Cordel Field, west central Alberta, and its relation to a nearby disposal well. *Journal of*
 481 *Geophysical Research: Solid Earth*, 119(4), 3410-3423.
- 482 Schultz, R., Wang, R., Gu, Y. J., Haug, K., & Atkinson, G. (2017). A seismological overview of
 483 the induced earthquakes in the Duvernay play near Fox Creek, Alberta. *Journal of*
 484 *Geophysical Research: Solid Earth*, 122(1), 492-505.
- 485 Shen, L. W., Schmitt, D. R., & Schultz, R. (2019). Frictional stabilities on induced earthquake
 486 fault planes at Fox Creek, Alberta: a pore fluid pressure dilemma. *Geophysical Research*
 487 *Letters*, 46(15), 8753-8762.

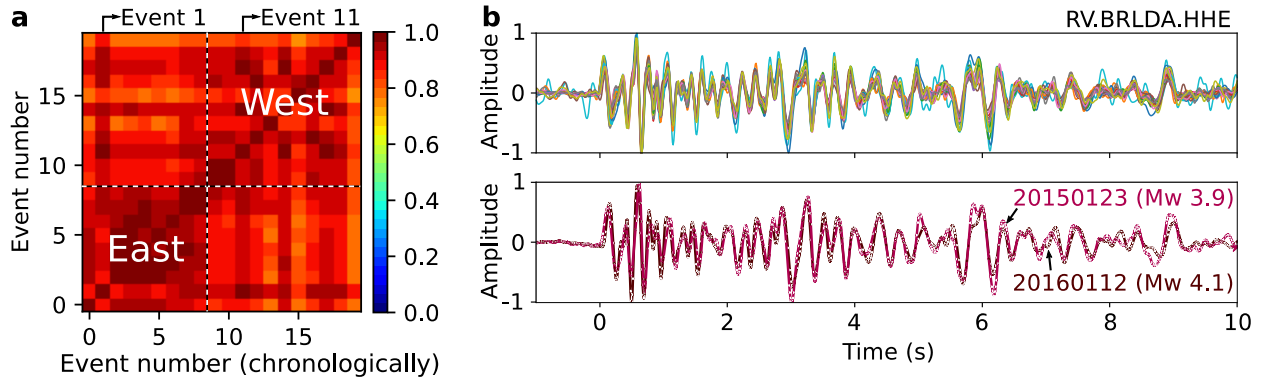
- 488 Stein, R. S. (1999). The role of stress transfer in earthquake occurrence. *Nature*, 402(6762), 605-
489 609.
- 490 Waldhauser, F., & Ellsworth, W. L. (2000). A double-difference earthquake location algorithm:
491 Method and application to the northern Hayward fault, California. *Bulletin of the*
492 *Seismological Society of America*, 90(6), 1353-1368.
- 493 Wang, B., Harrington, R. M., Liu, Y., Kao, H., & Yu, H. (2020). A study on the largest
494 hydraulic–fracturing–induced earthquake in Canada: Observations and static stress–drop
495 estimation. *Bulletin of the Seismological Society of America*, 110(5), 2283-2294.
- 496 Wang, B., Verdecchia, A., Kao, H., Harrington, R. M., Liu, Y., & Yu, H. (2021). A Study on the
497 Largest Hydraulic Fracturing Induced Earthquake in Canada: Numerical Modeling and
498 Triggering Mechanism. *Bulletin of the Seismological Society of America*.
- 499 Wang, R., & Kümpel, H. J. (2003). Poroelasticity: Efficient modeling of strongly coupled, slow
500 deformation processes in multilayered half-space. *Geophysics*, 68(2), 705-717.
- 501 Wang, R., Gu, Y. J., Schultz, R., Zhang, M., & Kim, A. (2017). Source characteristics and
502 geological implications of the January 2016 induced earthquake swarm near Crooked Lake,
503 Alberta. *Geophysical Journal International*, 210(2), 979-988.
- 504 Warren-Smith, E., Fry, B., Kaneko, Y., & Chamberlain, C. J. (2018). Foreshocks and delayed
505 triggering of the 2016 MW7. 1 Te Araroa earthquake and dynamic reinvigoration of its
506 aftershock sequence by the MW7. 8 Kaikōura earthquake, New Zealand. *Earth and Planetary*
507 *Science Letters*, 482, 265-276.
- 508 Warren–Smith, E., Chamberlain, C. J., Lamb, S., & Townend, J. (2017). High–precision
509 analysis of an aftershock sequence using matched–filter detection: The 4 May 2015 ML 6
510 Wanaka earthquake, Southern Alps, New Zealand. *Seismological Research Letters*, 88(4),
511 1065-1077.
- 512 Weingarten, M., Ge, S., Godt, J. W., Bekins, B. A., & Rubinstein, J. L. (2015). High-rate
513 injection is associated with the increase in US mid-continent seismicity. *Science*, 348(6241),
514 1336-1340.
- 515 Wilson, M. P., Worrall, F., Davies, R. J., & Almond, S. (2018). Fracking: How far from
516 faults?. *Geomechanics and Geophysics for Geo-Energy and Geo-Resources*, 4(2), 193-199.
- 517 Wolhart, S. L., Harting, T. A., Dahlem, J. E., Young, T., Mayerhofer, M. J., & Lolon, E. P.
518 (2006, January). Hydraulic fracture diagnostics used to optimize development in the Jonah
519 field. In *SPE Annual Technical Conference and Exhibition*. Society of Petroleum Engineers.
- 520 Xu, C., Wang, J., Li, Z., & Drummond, J. (2010). Applying the Coulomb failure function with an
521 optimally oriented plane to the 2008 Mw 7.9 Wenchuan earthquake
522 triggering. *Tectonophysics*, 491(1-4), 119-126.
- 523 Yamada, M., Mori, J., & Matsushi, Y. (2016). Possible stick–slip behavior before the Rausu
524 landslide inferred from repeating seismic events. *Geophysical Research Letters*, 43(17), 9038-
525 9044.
- 526 Yehya, A., Yang, Z., & Rice, J. R. (2018). Effect of fault architecture and permeability evolution
527 on response to fluid injection. *Journal of Geophysical Research: Solid Earth*, 123(11), 9982-
528 9997.

529 Yu, H., Harrington, R. M., Liu, Y., & Wang, B. (2019). Induced seismicity driven by fluid
530 diffusion revealed by a near-field hydraulic stimulation monitoring array in the Montney
531 Basin, British Columbia. *Journal of Geophysical Research: Solid Earth*, 124(5), 4694-4709.
532



533 **Figure 1.** Comparison of induced seismicity and HF activity. (a), Location of the 2015 Mw 3.9
 534 earthquake sequence in Fox Creek, Alberta, Canada. Beach balls of the 2015 Mw 3.9 and 2016
 535 Mw 4.1 events are taken from prior work (*Schultz et al., 2017*). The black square in the left panel
 536 shows the seismic station used in this study. In the right panel, solid lime bars denote the two
 537 fault strands of the 2015 sequence; dashed lime bar marks the hosted fault of the 2016 Mw 4.1
 538 event; triangles represent HF stages. (b), Injection history associated with the occurrence of
 539 induced earthquakes. The height of each colored bar represents the total volume of fluid injected
 540 at each stage while the width depicts the stage duration. In the bottom panel, stage ID is labelled
 541 above each treatment. In both (a) and (b), colored circles are the near-identical events (Figure 2);
 542 gray circles represent the uncorrelated small events; gray and pale green shaded areas represent
 543 P1 and P2 injection periods, respectively.

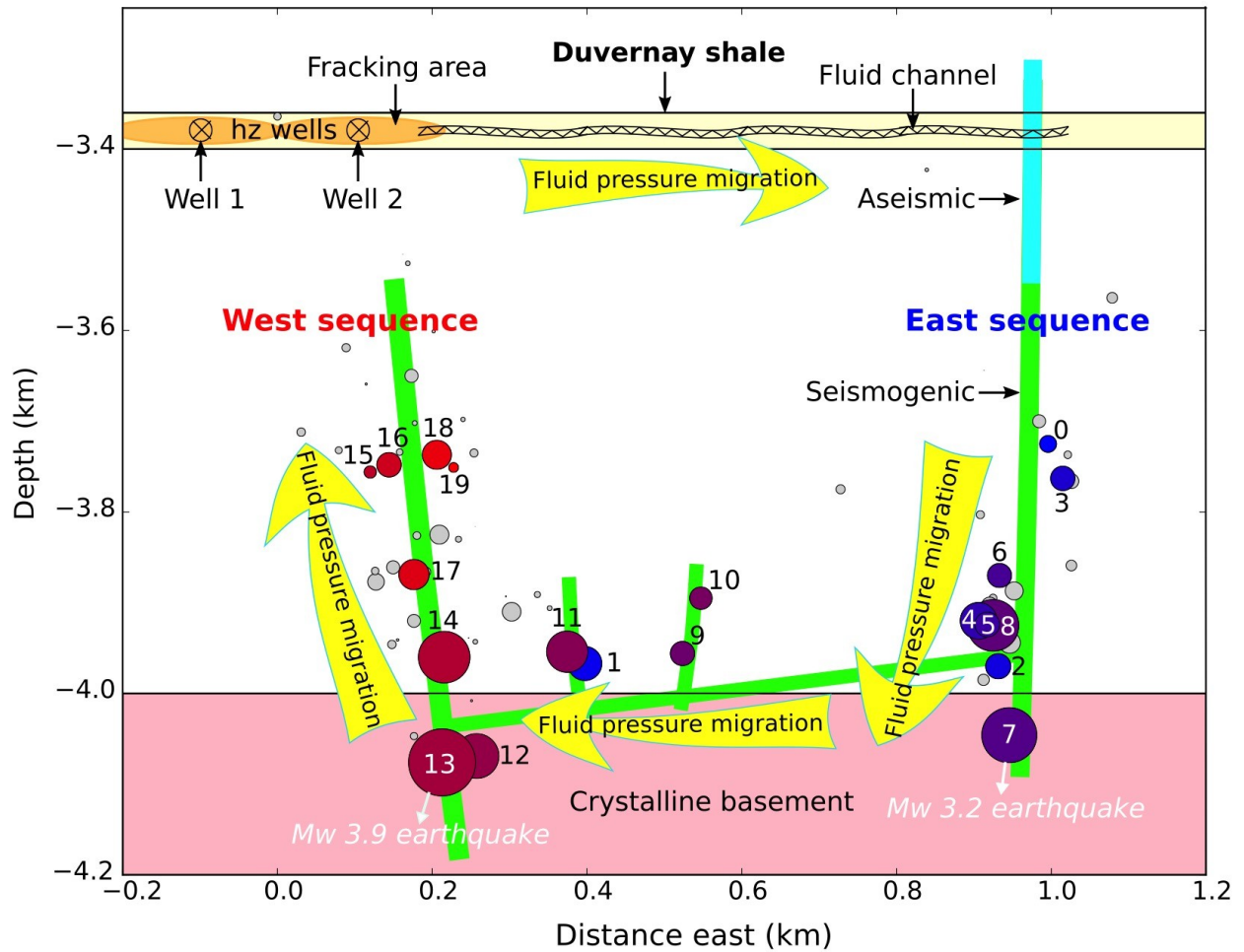
545
546
547



548
549
550
551
552
553

Figure 2. Identification of near-identical earthquakes. (a) Cross-correlation matrix of 20 correlated events (i.e., near-identical earthquakes). (b) Normalized waveforms of the 20 near-identical earthquakes (top panel) and of the two large events (bottom panel).

554



555
 556 **Figure 3.** East-west cross section of the 2015 Mw 3.9 earthquake sequence. 20 correlated events
 557 are marked by numbered and color-coded circles, with the smaller numbers and cooler colors
 558 corresponding to earlier events. Gray circles represent the 49 poorly correlated events. Circle
 559 sizes are scaled according to earthquake magnitudes. Crossed circles mark two HF horizontal
 560 wells.
 561
 562

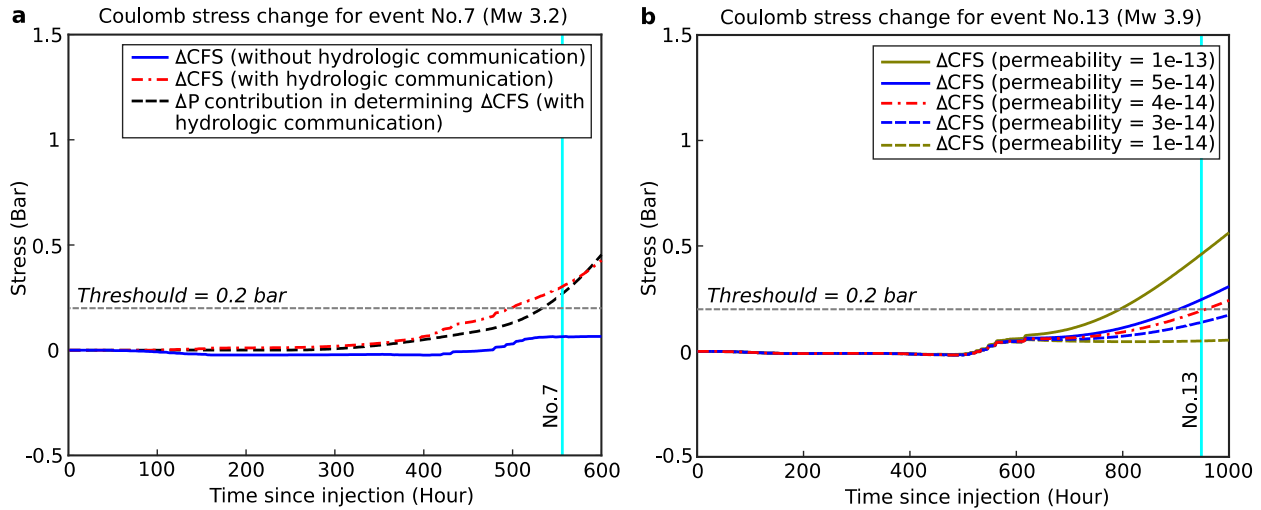
563
564565
566
567
568
569
570
571
572
573

Figure 4. Poroelastic modeling results for the Mw 3.2 event (a) and Mw 3.9 event (b). Vertical cyan lines mark the origin times of the two earthquakes. Note for (b), the results of using a permeability lower than $1 \times 10^{-14} \text{ m}^2$ are nearly identical to that of $1 \times 10^{-14} \text{ m}^2$ and hence are not displayed for simplicity. In such low permeability cases, the ΔP contribution in determining the ΔCFS for the Mw 3.9 event is negligible as the fluid pressure can not reach the west sequence fault for the observed time scale. The corresponding ΔP contributions of using different permeabilities in (b) are given in Figure S2.